Alexandria Engineering Journal 105 (2024) 156–169

Contents lists available at ScienceDirect

Alexandria Engineering Journal

journal homepage: www.elsevier.com/locate/aej

Mechanical properties and insulation damage of PMSG stator end windings with eccentricity considerations

De-Rui Dai [a], Yu-Ling He [a,b,*,1], Ming-Xing Xu [a], Wen Zhang [a], Zi-Xiang Fu [a], David Gerada [c]

[a] The Hebei Key Laboratory of Electric Machinery Maintenance and Failure Prevention, North China Electric Power University, Baoding 071003, China
[b] Suzhou Research Institute, North China Electric Power University, Suzhou 215123, China
[c] Department of Electrical and Electronic Engineering, University of Nottingham, University Park NG7 2RD, UK

ARTICLE INFO

Keywords:
permanent magnet synchronous generator (PMSG)
end windings
eccentricity
mechanical characteristics
insulation damage

ABSTRACT

The mechanical properties and insulation damage of stator end windings in permanent magnet synchronous generator (PMSG) are investigated by theoretical analysis, finite element analysis (FEA) and experiment verification. First, a theoretical model of the winding electromagnetic force (EF) and vibration response before and after eccentricity faults are established. Then, the stress/strain distribution of the end windings under different working conditions is analyzed. Finally, the insulation damage behavior of end windings with initial cracks is studied and characterized using the stress intensity factor (SIF). The results indicate that the winding EF and vibration responses vary under different faults. The stress/strain at the joint of the winding is the largest, and the insulation layer has the maximum stress/strain under the same section. Additionally, the SIF amplitude of the crack at the winding joint is the largest. And the SIF amplitude of the crack will increase with the increase of fault degree/crack depth/crack length. The contribution of this paper lies in the comprehensive analysis of the winding EF distribution, vibration response, stress and strain, and insulation damage before and after eccentricity. This analysis can provide valuable reference for the health monitoring of PMSG eccentricity faults and the prevention of winding insulation damage.

1. Introduction

Electricity stands as the fundamental cornerstone of modern society, with generators playing a pivotal role in its generation. Notably, permanent magnet synchronous generators (PMSGs) have become essential components in the renewable energy sector, especially in the fast-growing field of wind energy [1–3]. The global installed capacity of wind turbines has been steadily increasing every year [4], underscoring the critical role of PMSG performance in maintaining the stability and sustainability of energy production [5]. The insulation of the stator winding is an extremely crucial component for ensuring the reliable operation of all electric machines [6]. In fact, statistics reveal that one-third of forced shutdowns of large generators are attributed to failures in the stator winding's insulation system [7]. As a result, it is of paramount significance to investigate the mechanical properties and insulation damage mechanism of PMSG stator winding.

Numerous scholars have delved into the mechanical properties of generator windings. The winding, being a pivotal component for energy conversion in generators, is subject to the continuous influence of time-varying electromagnetic force (EF) during operation [8]. The end winding is more susceptible to damage from EF due to its distinctive cantilever structure [9]. Bingjie Jing et al. analyzed the transient EF of the electric machines end winding during dynamic reactive power compensation process [10]. Reference [11] employed finite element analysis (FEA) to calculate the EF at the end winding of generators. In reference [12], a novel numerical approach to calculate end winding EF of large turbine generators is presented.

Furthermore, the vibration of end windings induced by

Abbreviation: PMSG, Permanent magnet synchronous generator; SAGE, Static air-gap eccentricity; HAGE, Hybrid air-gap eccentricity; FEA, Finite element analysis; MMF, Magnetomotive force; EF, Electromagnetic force; DAGE, Dynamic air-gap eccentricity; SIF, Stress intensity factor; MFD, Magnetic flux density; PPUA, Permeance per unit area.

* Corresponding author at: The Hebei Key Laboratory of Electric Machinery Maintenance and Failure Prevention, North China Electric Power University, Baoding 071003, China.
E-mail address: heyuling1@163.com (Y.-L. He).

[1] https://doi.org/10.1016/j.ijepes.2021.00.000

https://doi.org/10.1016/j.aej.2024.06.090
Received 31 March 2024; Received in revised form 7 June 2024; Accepted 28 June 2024
Available online 4 July 2024
1110-0168/© 2024 The Author(s). Published by Elsevier BV on behalf of Faculty of Engineering, Alexandria University This is an open access article under the CC BY-NC-ND license (http://creativecommons.org/licenses/by-nc-nd/4.0/).

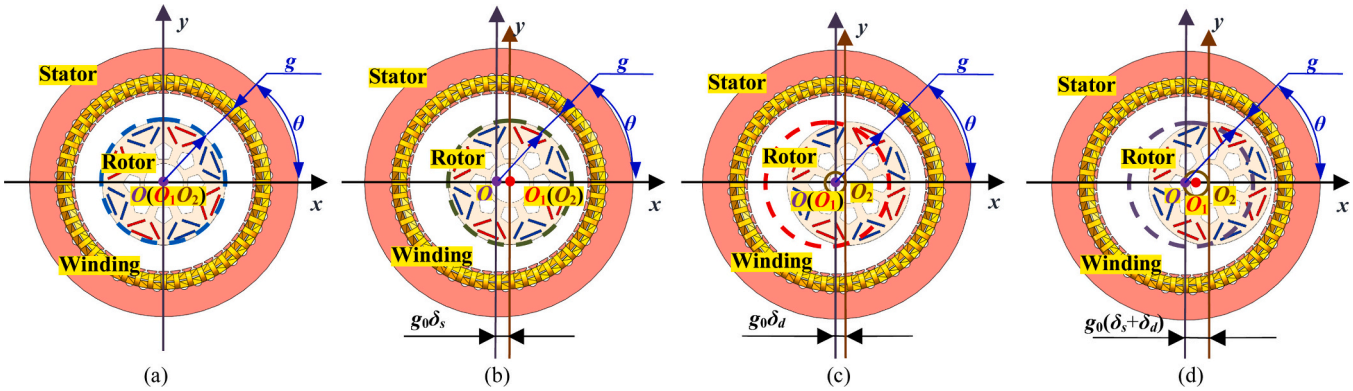

Fig. 1. Air-gap of PMSG (a) Normal, (b) SAGE, (c) DAGE, (d) HAGE.

electromagnetic forces (EF) is a significant concern. Juan Li et al. analyzed the influence of various parameters on the vibration characteristics of stator end windings through parametric modeling [13]. P. Kung, L. et al. utilized fiber optic sensors to monitor the vibration of generator end windings [14]. Ying Zhou et al. investigated the dynamic characteristics of the end windings through FEA [15]. The stress and strain experienced by the windings also warrant attention. Y. Fang et al. conducted the stress analysis of the electrical submersible motor end windings [16]. Haijun Zhang et al. studied the stress and deformation of the end winding under the influence of EF [17]. These studies shed light on the mechanical challenges faced by windings in electric machines.

The insulation layer is a crucial element of windings, and its damage is one of leading factors in electrical machine accidents [18,19]. The primary types of stress and strain that affect the degradation of the stator insulation system include mechanical, thermal, voltage and environmental factors [20–23]. This paper specifically examines the impact of winding EF on insulation, a form of mechanical damage to insulation. Prior to this, K. Kimura et al. conducted mechanical fatigue experiments on insulation and carried out crack observation work [24]. Xiaolin Chen et al. designed a mechanical aging device to simulate the vibration stress of winding insulation [25]. Aditya Gokhale et al. studied the cracks and fractures in windings [26]. Haijun Zhang et al. analyzed the insulating layer behavior considering the initial crack defect of the end winding and the end hoop support failure by FEA [17].

Regrettably, the aforementioned studies are grounded in the assumption of normal operation for electric machines. In fact, the vast majority of generators are “operating with illness”. Manufacturing and assembly errors often result in generators having a certain degree of eccentricity fault, and prolonged operation, subject to mechanical, electromagnetic, thermal, and other forces, tends to exacerbate the level of eccentricity [27,28]. The air-gap eccentricity fault can be categorized into three cases: static air-gap eccentricity (SAGE), dynamic air-gap eccentricity (DAGE) and hybrid air-gap eccentricity (HAGE) [29].

Scholars have done a lot of research on air-gap eccentricity. Yao Da et al. analyzed the magnetic field characteristics of the motor under eccentricity and detected faults using search coils [30]. Yu-Ling He et al. achieved a non-invasive measurement of SAGE position by utilizing external search coils [31]. Monitored electrical parameters also serve as effective indicators for assessing the condition of electric machines [32–34]. Bashir Mahdi Ebrahimi et al. analyzed the degree of DAGE fault in motors by examining the stator current spectrum and torque [35]. Estefania Artigao et al. diagnosed DAGE faults in generators by analyzing current characteristics [36]. Detecting eccentricity through the vibration characteristics of key generator components is another effective approach. Various schemes for detecting eccentricity by analyzing the vibration of stators [37,38], rotors [39], and windings [40] have been proposed consecutively. However, it’s essential to highlight that the analysis of vibration characteristics in PMSG end windings under SAGE, DAGE, and HAGE faults is currently lacking. Additionally, Alessandro Cimino conducted insulation aging tests under mechanical stress [41], and he introduced the effect of cyclic mechanical stress on the aging of stator winding insulation systems [42]. But the mechanical failure characteristics of winding insulation under abnormal conditions such as eccentricity have not been analyzed.

This paper presents a comprehensive study on the mechanical properties and insulation damage of PMSG stator end windings both before and after eccentricity. The main innovations are as follows: 1) This paper not only examines the mechanical properties of end windings under normal condition but also delves into the mechanical characteristics under SAGE, DAGE and HAGE. In addition to exploring the time-domain and frequency-domain characteristics of winding EF and vibration responses, the spatial distribution of EF is thoroughly investigated. 2) The stress and strain of the end winding before and after the eccentricity are analyzed, and the dangerous position of the end winding is found out. In addition, the stress and strain distribution inside the end winding is investigated. 3) This paper also delves into the analysis of insulation layer fractures, taking into account various factors including the presence of eccentric faults, the location of cracks, as well as the depth and length of the crack. The research presented in this paper is valuable for identifying potential failure points in PMSGs beforehand, offering guidance for daily maintenance and overhauls of wind turbines, and enhancing the reliability and safety of wind turbine operations.

The remainder of the paper is organized as follows. In the Section 2, the theoretical model of PMSG end winding mechanical properties and insulation crack analysis is established. In the Section 3, the theory is verified and further explored through FEA and experimental research. Finally, the main conclusions of this research are outlined in Section 4.

2. Theoretical model

2.1. Electromagnetic force and vibration analysis of end windings

In order to simplify the theoretical analysis of PMSG, it is assumed that: 1) the influence of the stator core slot and the influence of the end effect are ignored, 2) ignore the influence of magnetic saturation effect, 3) the stator is rigid constraint, and the vibration transmission problem of rotor-stator and stator-winding is ignored.

The air-gap magnetic flux density (MFD) of PMSG is determined by the product of magnetomotive force (MMF) and permeance per unit area (PPUA). The influence of eccentricity faults on MMF is minimal and can be disregarded. Therefore, the expression for MMF under both normal and eccentricity faults is as follows:

$$\begin{cases} f(\theta,t) = f_R(\theta,t) + f_S(\theta,t) \\ f_R(\theta,t) = \sum_{\mu} F_\mu \cos\left(\mu p\theta - \mu\omega t - \phi_\mu\right), \mu = 2m+1, m = 0,1,2\ldots \\ f_S(\theta,t) = \sum_{\upsilon} F_\upsilon \cos(\upsilon p\theta - \omega t - \phi_\upsilon), \upsilon = 6n+1, n = 0,\pm1,\pm2\ldots \end{cases} \tag{1}$$

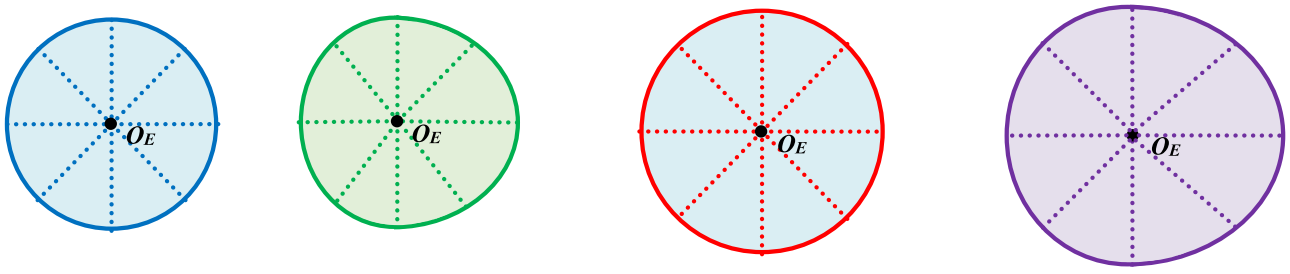

Fig. 2. EF of PMSG (a) Normal, (b) SAGE, (c) DAGE, (d) HAGE.

where $f(\theta,t)$ is the synthetic MMF, $f_S(\theta,t)$ and $f_R(\theta,t)$ respectively represent the MMF generated by the stator winding magnetic field and the rotor magnetic field. F_μ and F_υ represent the μ-harmonic MMF of permanent magnet and the υ-harmonic MMF of stator winding, respectively. ϕ_μ and ϕ_υ represent the initial phase angle of the MMF of the μ-harmonic wave of the permanent magnet and the υ-harmonic MMF of the stator winding, respectively. θ is the mechanical position angle. p is the number of generator pole pairs. $\omega=2\pi f$, f is the frequency of power generation (f=50 Hz in this manuscript).

Eccentricity faults affect the air-gap length, which in turn affects the PPUA. The various types of eccentricity faults are represented in Fig. 1.

Under normal circumstances, the geometrical center O of the stator and the rotational center O_1 of the rotor are consistent with the geometrical center O_2 of the rotor, resulting in an even distribution of the air-gap in the PMSG, as depicted in Fig. 1(a). The SAGE faults occur when O_1 and O_2 still coincide but deviate from the stator's geometrical center O. The offset distance is the SAGE degree. At this time, one side of the air-gap increases and the other side decreases, as shown in Fig. 1(b). DAGE faults take place when the stator's geometrical center O continues to coincide with the rotor's rotational center O_1, but the rotor shafting (i.e., rotor's geometrical center O_2) shifts. The offset distance represents the DAGE degree, as illustrated in Fig. 1(c). The HAGE fault is a combination of SAGE and DAGE. In this case, O, O_1, and O_2 no longer coincide. The distance from O_1 to O is the SAGE degree, the distance between O_2 and O_1 indicates the DAGE degree, and the HAGE degree is the compound of SAGE and DAGE, as presented in Fig. 1(d).

Consequently, the air-gap length before and after the occurrence of eccentricity is represented in (2).

$$g=\begin{cases} g_0 \cdots\cdots Normal \\ g_0\left(1-\delta_s\cos\theta\right) \cdots\cdots SAGE \\ g_0\left[1-\delta_d\cos(\theta-\omega_r t-\phi_0)\right] \cdots\cdots DAGE \\ g_0\left[1-\delta_s\cos\theta-\delta_d\cos(\theta-\omega_r t-\phi_0)\right] \cdots\cdots HAGE \end{cases} \tag{2}$$

where g_0 is the uniform air-gap length under normal condition. δ_s and δ_d are the value of static eccentricity and dynamic eccentricity, respectively. ω_r is the angular speed of the rotor, $\omega_r=2\pi f_r$, f_r is the rotor rotation frequency (f_r=12.5 Hz in this manuscript).

The PPUA under each operational condition is as follows:

$$\Lambda(\theta)=\mu_0/g=\begin{cases} \Lambda_0 \cdots\cdots Normal \\ \Lambda_0(1+\delta_s\cos\theta) \cdots\cdots SAGE \\ \Lambda_0(1+\delta_d\cos(\theta-\omega_r t-\phi_0)) \cdots\cdots DAGE \\ \Lambda_0(1+\delta_s\cos\theta+\delta_d\cos(\theta-\omega_r t-\phi_0)) \cdots HAGE \end{cases} \tag{3}$$

where μ_0 is air permeability.

According to (3), the PPUA decreases in locations where the air-gap increases, and it increases in positions where the air-gap decreases.

Based on (1) and (3), the expression of MFD is:

$$B(\theta,t)=f(\theta,t)\Lambda(\theta)$$

$$=\begin{cases} \Lambda_0\sum_\mu F_\mu\cos\left(\mu\omega t-\mu p\theta+\phi_\mu\right)+\Lambda_0\sum_\upsilon F_\upsilon\cos(\omega t-\upsilon p\theta+\phi_\upsilon)=B_{XN} \cdots\cdots Normal \\ B_{XN}+\dfrac{\Lambda_0\delta_s}{2}\sum_\mu F_\mu\cos\left[\mu\omega t-\left(\mu p\pm 1\right)\theta+\phi_\mu\right]+\dfrac{\Lambda_0\delta_s}{2}\sum_\upsilon F_\upsilon\cos\left[\omega t-\left(\upsilon p\pm 1\right)\theta+\phi_\upsilon\right]=B_{XN}+B_{XSe} \cdots SAGE \\ B_{XN}+\dfrac{\Lambda_0\delta_d}{2}\sum_\mu F_\mu\cos\left(\left(\mu\omega\pm\omega_r\right)t-\left(\mu p\pm 1\right)\theta+\left(\phi_\mu\pm\phi_0\right)\right) \\ +\dfrac{\Lambda_0\delta_d}{2}\sum_\upsilon F_\upsilon\cos((\omega\pm\omega_r)t-(\upsilon p\pm 1)\theta+(\phi_\upsilon\pm\phi_0))=B_{XN}+B_{XDe} \cdots\cdots DAGE \\ B_{XN}+B_{XSe}+B_{XDe} \cdots\cdots HAGE \end{cases} \tag{4}$$

The stator end winding EF can be calculated by (5) [40].

$$\begin{aligned} F\left(\theta,t\right) &= \int_0^l B_l(\theta,t)i\cos(\alpha_l)\sin(\beta_l)dl \\ &= \int_0^l B_l(\theta,t)[B(\theta,t)Lv/Z]\cos(\alpha_l)\sin(\beta_l)dl \\ &= \eta B^2\left(\theta,t\right)Llv/Z \end{aligned} \tag{5}$$

where $B_l(\theta,t)$ is the MFD at the end of the generator, which is the product

of $B(\theta,t)$ and the weakening coefficient η, where $0<\eta<1$, i is the stator winding current, L is the length of the straight section winding, l is the axial length of the end winding, α_l is the angle between the MFD at a point in the end winding and the point normal, β_l is the angle between the normal at a point in the end winding and the axis of the rotor. v is the speed at which the linear winding cuts the magnetic inductance line, and Z is the impedance of the winding.

Feeding (4) into (5), the concrete end winding EF expression can be obtained:

$$F(\theta,t)=\begin{cases}\dfrac{\eta Llv\Lambda_0^2}{2Z}\{\sum_{\mu_1}\sum_{\mu_2}F_{\mu_1}F_{\mu_2}\cos[(\mu_1\pm\mu_2)\omega t-(\mu_1\pm\mu_2)p\theta+(\phi_{\mu_1}\pm\phi_{\mu_2})]+2\sum_{\mu}\sum_{\upsilon}F_{\mu}F_{\upsilon}\cos[(\mu\pm1)\omega t-(\mu\pm\upsilon)p\theta+(\phi_{\mu}\pm\phi_{\upsilon})]\\ +\sum_{\upsilon_1}\sum_{\upsilon_2}F_{\upsilon_1}F_{\upsilon_2}\cos[(\omega\pm\omega)t-(\upsilon_1p\pm\upsilon_2p)\theta+(\phi_{\upsilon_1}\pm\phi_{\upsilon_2})]\}=F_{XN}\cdots\cdots Normal\\ F_{XN}+\dfrac{\eta Llv\Lambda_0^2\delta_s}{2Z}\{\sum_{\mu_1}\sum_{\mu_2}F_{\mu_1}F_{\mu_2}\cos[(\mu_1\pm\mu_2)\omega t-(\mu_1p\pm(\mu_2p\pm1))\theta+(\phi_{\mu_1}\pm\phi_{\mu_2})]\\ +2\sum_{\mu}\sum_{\upsilon}F_{\mu}F_{\upsilon}\cos[(\mu\pm1)\omega t-(\mu p\pm(\upsilon p\pm1))\theta+(\phi_{\mu}\pm\phi_{\upsilon})]\\ +\sum_{\upsilon_1}\sum_{\upsilon_2}F_{\upsilon_1}F_{\upsilon_2}\cos[(\omega\pm\omega)t-(\upsilon_1p\pm(\upsilon_2p\pm1))\theta+(\phi_{\upsilon_1}\pm\phi_{\upsilon_2})]\}=F_{XN}+F_{XSe}\cdots\cdots SAGE\\ F_{XN}+\dfrac{\eta Llv\Lambda_0^2\delta_d}{2Z}\{\sum_{\mu_1}\sum_{\mu_2}F_{\mu_1}F_{\mu_2}\cos[(\mu_1\omega\pm(\mu_2\omega\pm\omega_r))t-(\mu_1p\pm(\mu_2p\pm1))\theta+(\phi_{\mu_1}\pm(\phi_{\mu_2}\pm\phi_0))]\\ +2\sum_{\mu}\sum_{\upsilon}F_{\mu}F_{\upsilon}\cos[(\mu\omega\pm(\omega\pm\omega_r))t-(\mu p\pm(\upsilon p\pm1))\theta+(\phi_{\mu}\pm(\phi_{\upsilon}\pm\phi_0))]\\ +\sum_{\upsilon_1}\sum_{\upsilon_2}F_{\upsilon_1}F_{\upsilon_2}\cos[(\omega\pm(\omega\pm\omega_r))t-(\upsilon_1p\pm(\upsilon_2p\pm1))\theta+(\phi_{\upsilon_1}\pm(\phi_{\upsilon_2}\pm\phi_0))]\}=F_{XN}+F_{XDe}\cdots\cdots DAGE\\ F_{XN}+F_{XSe}+F_{XDe}\cdots\cdots HAGE\end{cases}\tag{6}$$

According to (6), the frequency components of the stator winding EF under normal and SAGE faults are $(\mu_1\pm\mu_2)f$. However, when DAGE and HAGE are present, additional sideband frequencies of $(\mu_1\pm\mu_2)f\pm f_r$ appear in addition to the original components.

Fig. 2 shows the spatial distribution of EF in each winding calculated by the theoretical model. According to Fig. 2, the spatial distribution of EF undergoes changes before and after the eccentricity. The dashed line distance from O_E to the circle's edge represents the amplitude of EF at the corresponding winding position. Under normal condition, EF is evenly distributed across the windings, meaning the EF amplitude for each winding is the same, as depicted in Fig. 2(a). The occurrence of SAGE faults will cause uneven distribution of EF. Specifically, EF increases in regions where the air-gap decreases and decreases where the air-gap increases, as presented in Fig. 2(b). After DAGE faults occur, the EF amplitude for each winding position uniformly increases, as seen in Fig. 2(c). HAGE faults represent the superposition of SAGE and DAGE, as shown in Fig. 2(d).

The straight section of the windings in the PMSG is firmly anchored within the stator core, with the end part extending outward, as illustrated in Fig. 3(a). The end of the winding takes on the characteristics of a cantilever beam structure, making it particularly vulnerable to the presence of the EF. Consequently, this paper places a specific emphasis on the vibration and insulation damage occurring in the end winding.

As depicted in Fig. 3(b), the end winding is segmented into three parts: the joint part connected to the stator core, the involute part in the middle, and the nose end at the extremity. And the end winding is subjected to an uneven distribution of EF. Fig. 3(c) provides the mechanical model of the end winding. Consequently, the mechanical expression describing the vibration of the end winding under EF can be formulated as (7).

$$\{[m]\{\boldsymbol{y}''(t)\}+[D]\{\boldsymbol{y}'(t)\}+[K]\{y(t)\}=\{F(\theta,t)\}\tag{7}$$

where $[m]$ represents the matrix of the stator end winding mass point, $[D]$ represents the damping matrix in radial direction, $[K]$ represents the stiffness matrix in radial direction. $y(t)$ is the displacement of the unit mass point, $y'(t)$ is the speed, $y''(t)$ are the acceleration.

As indicated in (7), according to the same frequency correspondence relation between the exciting force and the movement, the vibration should have the same frequency/harmonic components as the EF.

2.2. Stress and strain analysis of end windings

Eq. (6) is the overall EF expression of the end windings. To calculate stress and strain, it's essential to work with the local EF, which is the EF density. EF density is the macroscopic representation of the Lorentz force acting on the charged particles within the winding, and its expression is as follows:

$$\rho=i\times B_l(\theta,t)\tag{8}$$

Given that the primary direction of the EF is radial, this paper focuses solely on the radial component of EF. And the distribution of stress (σ_m) and strain (ε) within the end winding can be calculated based on the EF density, as illustrated in (9) and Fig. 4.

$$\begin{aligned}&\sigma_m=My\Big/I_z=y_c\int_0^x F_s dx\Big/I_z=y_c\int_0^x\int_0^x\rho dxdx\Big/I_z\\&\varepsilon=\sigma_m/E\end{aligned}\tag{9}$$

where M is the bending moment of the section, y_c is the distance from the point of the section to the neutral axis, I_z is the moment of inertia, x is the distance from the end of the winding to the analyzed section, F_s is the sheer force of the section, and E is the Young's Modulus of elasticity of the material.

As depicted in Fig. 4(a), the straight section of the windings is fixed and constrained by the stator core, while the end winding remains suspended. EF is distributed unevenly in the end winding. The farther move from the nose end, the greater the accumulated bending moment, resulting in higher cross-sectional stress. Consequently, the stress at the joint of the winding is more pronounced.

Fig. 4(b) illustrates a section of the end winding, and its stress distribution aligns with the described in (9). Specifically, the farther move from the neutral axis, the greater the stress with the winding. The insulation layer, located on the outermost part of the winding, is subject to higher stress levels due to its position. Additionally, the stress distribution of the insulation layer (σ_{mi}) gradually decreases from the outside to the inside.

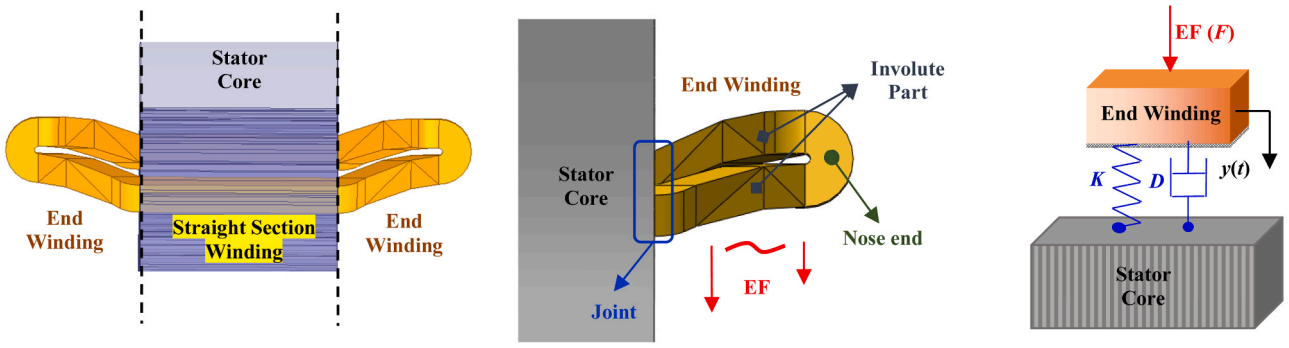

Fig. 3. Stator-winding system (a) Stator-winding structure, (b) End winding structure, (c) Mechanical model of the end winding.

2.3. Insulation failure analysis

The stress within the thin insulation layer is almost uniform during PMSG operation. This paper assumes that the stress in the insulation layer at the same side of the same section are equal, meaning that the stress within the insulation layer $\sigma_{mi} = \sigma_y$, as demonstrated in Fig. 5.

The insulation damage analysis conducted in this study is based on the assumption that there exists an initial crack on the surface of the winding's insulation, as demonstrated in Fig. 4(a). Under the influence of the EF, the predominant type of insulation damage is open-type (type I) cracks, as displayed in Fig. 5. To quantitatively assess the stress field at the crack tip, the stress intensity factor (SIF) is introduced. Subsequently, the study examines the damage behavior of EF on insulation in the presence of an initial crack defect, as described in (10).

$$\begin{cases} \sigma_x = \dfrac{K_1}{\sqrt{2\pi r}} \cos\dfrac{\theta_c}{2}\left(1 - \sin\dfrac{\theta_c}{2}\sin\dfrac{3\theta_c}{2}\right) \\ \sigma_y = \dfrac{K_1}{\sqrt{2\pi r}} \cos\dfrac{\theta_c}{2}\left(1 + \sin\dfrac{\theta_c}{2}\sin\dfrac{3\theta_c}{2}\right) \\ \tau_{xy} = \dfrac{K_1}{\sqrt{2\pi r}} \cos\dfrac{\theta_c}{2}\sin\dfrac{\theta_c}{2}\cos\dfrac{3\theta_c}{2} \end{cases} \tag{10}$$

where σ_x and σ_y are the far-field stress in the x direction and y direction respectively, τ_{xy} is the far-field shear stress, K_1 is the type I SIF, r and θ_c are the polar coordinates of the crack tip.

The expression of SIF is:

$$K_1 = \sigma_y\sqrt{2\pi a} \tag{11}$$

where a is the depth of crack.

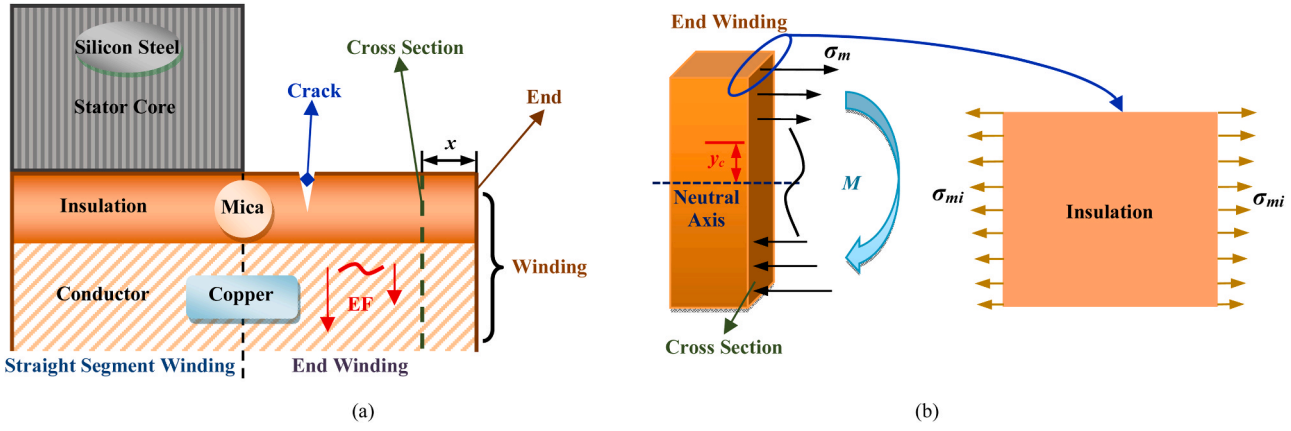

Fig. 4. Winding structure and stress (a) Winding structure, (b) Section stress distribution.

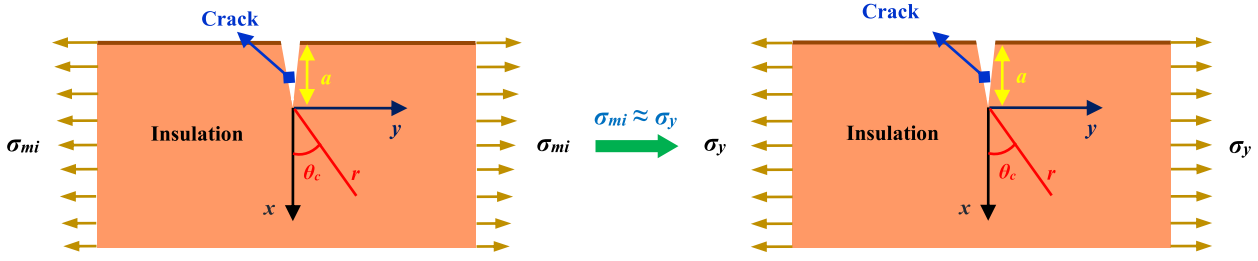

Fig. 5. Insulation layer stress and crack coordinate system.

Table 1
Key parameters of PMSG.

Parameter	Value	Parameter	Value
Rated capacity	3 kW	Rated speed	n_r=750 r/min
Stator slots	Z_s=48	Stator length	l_s=40 mm
Air-gap length	g_0=1.2 mm	Pitch coefficient	k_y=0.83
Pole pairs	p=4	Parallel branches	N_{pb}=2

A higher SIF indicates a greater stress concentration at the crack front, which, in turn, increases the propensity for crack propagation. The amplitude of SIF is influenced by various factors, including the size of the EF, the location and size of cracks, among others. These specific influences will be further analyzed through FEA.

3. FEA and experimental verification

3.1. Electromagnetic force and vibration verification of end windings

3.1.1. FEA and experimental setup

FEA and experiments were conducted on a 3 kW PMSG. The detailed parameters of PMSG can be found in Table 1. The main assumptions in the FEA are as follows: 1) the PMSG material is homogeneous and isotropic, 2) the rotor geometry is smooth, 3) the components of PMSG are treated as a continuum rather than discrete atoms or molecules, 4) the internal structure of the PMSG has no initial stress. Fig. 6, Fig. 7 and Fig. 8 provide an overview of the FEA setup, experimental setup and experimental eccentricity setup, respectively.

In the Ansys Electronics software, the FEA body model of PMSG under normal working conditions was created, as depicted in Fig. 6(a). The excitation of the model winding is achieved through the external

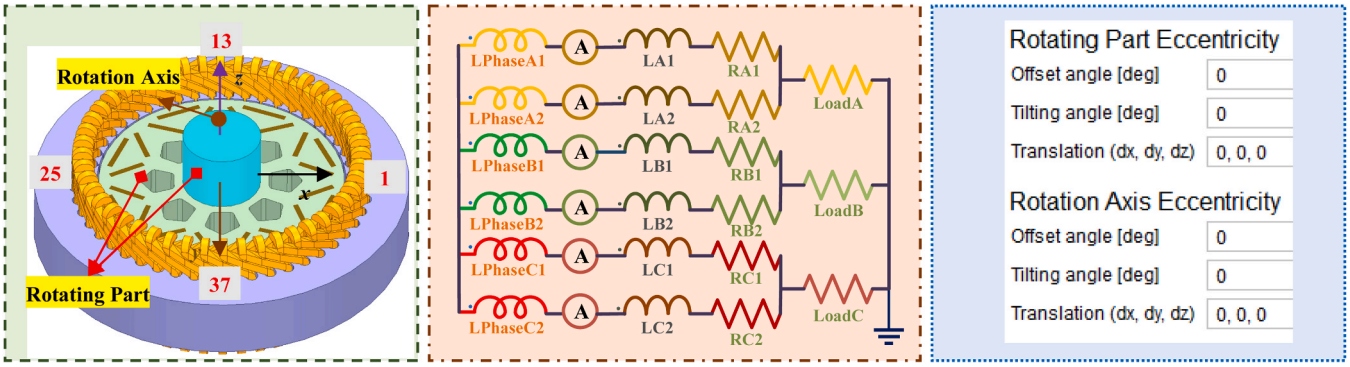

(a) (b) (c)

Fig. 6. FEA setup (a) PMSG model, (b) External circuit model, (c) Eccentricity setup.

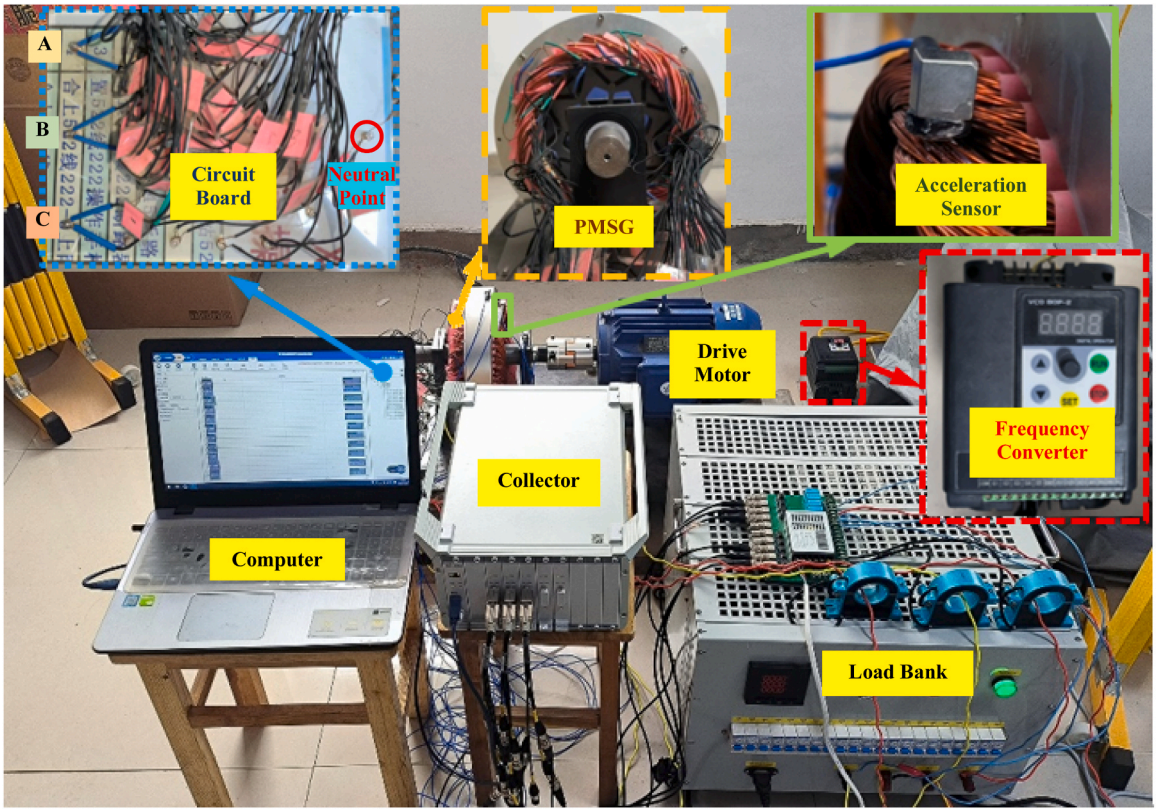

Fig. 7. Experimental setup.

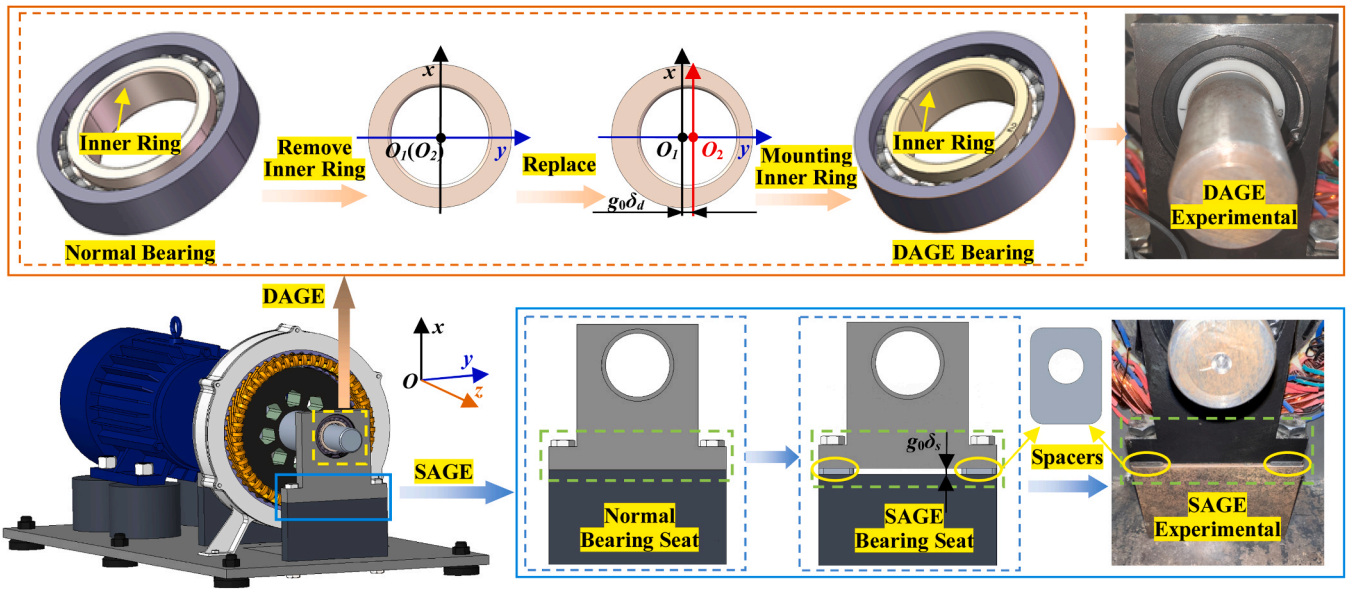

Fig. 8. Experimental eccentricity setup.

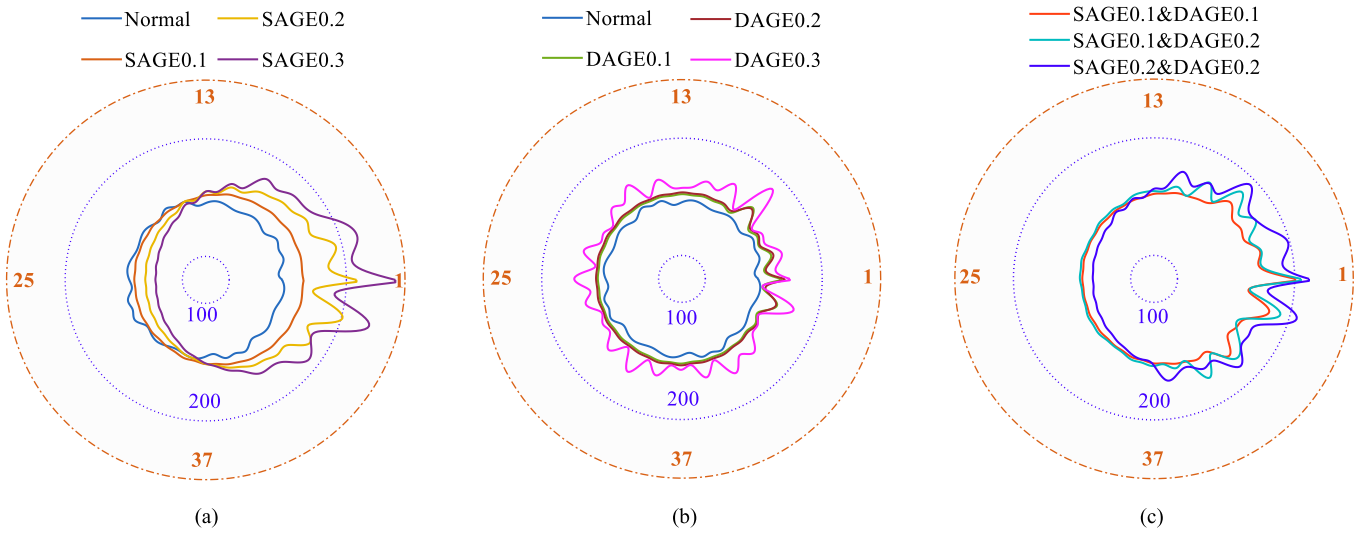

Fig. 9. EF distribution of PMSG winding (a) Normal and SAGE, (b) Normal and DAGE, (c) HAGE.

circuit, and the configuration of the model's external circuit aligns with the experimental setup, as shown in Fig. 6(b) and Fig. 7.

The setting of the eccentric fault is automatically set by ACT, as demonstrated in Fig. 6(c). Specifically, to simulate SAGE, both the "Rotating Part" and the "Rotating Axis" are adjusted, causing a shift in both the rotor system and the center of rotation simultaneously. To simulate DAGE, only the "Rotating Part" needs to be adjusted, creating a situation where the geometric center of the rotor no longer coincides with the rotating center. Various degrees of HAGE can be achieved by adjusting the fault degrees of SAGE and DAGE separately. It's important to note that in this paper, both SAGE and DAGE offset in the forward direction along the *x*-axis. Consequently, the air-gap in winding 1 is the

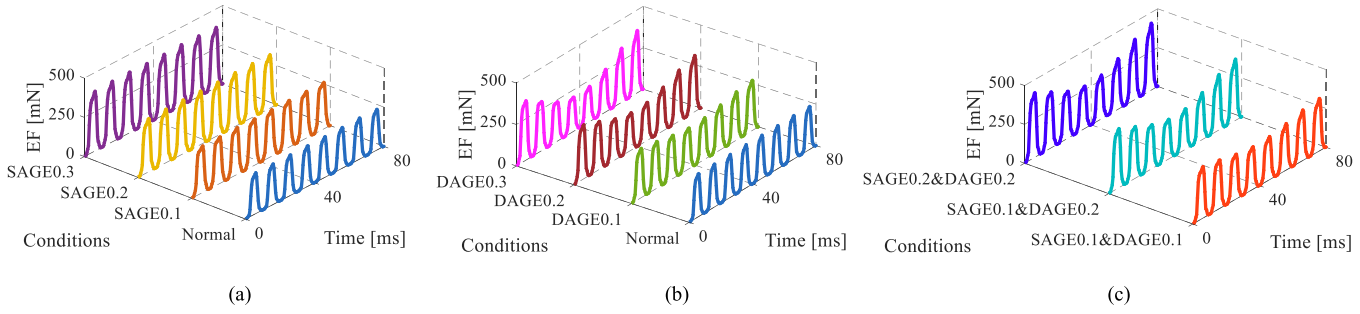

Fig. 10. Time domain of stator winding EF (a) Normal and SAGE, (b) Normal and DAGE, (c) HAGE.

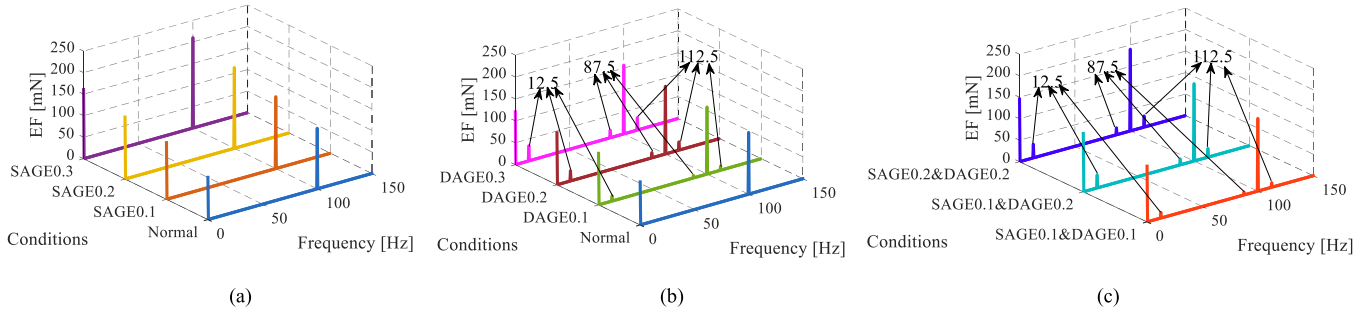

Fig. 11. Frequency domain of stator winding EF (a) Normal and SAGE, (b) Normal and DAGE, (c) HAGE.

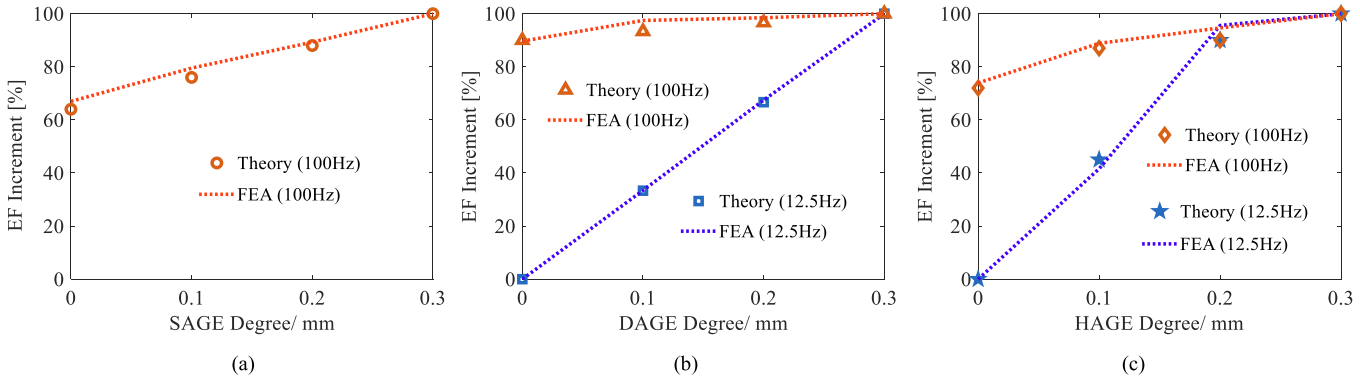

Fig. 12. Comparison of theory and FEA results (a) Normal and SAGE, (b) Normal and DAGE, (c) Normal and HAGE.

smallest after the occurrence of SAGE fault, as displayed in Fig. 6(a).

As depicted in Fig. 7, during the experiment, the frequency converter controls the speed of the drive motor, and the motor drives the PMSG rotor to rotate through the elastic coupling. The electrical energy generated by the PMSG is converted into heat energy through the load bank (full load condition). The PMSG windings have a double Y-type connection, maintaining consistency with the FEA model. The vibration acceleration sensor is installed on the stator winding 1, and the signals it records are transmitted to a computer via the data collector for subsequent data analysis.

The experimental eccentricity setup is illustrated in Fig. 8. To introduce SAGE, spacers are inserted between the bearing housings. In contrast, to introduce DAGE, the inner ring of the bearing is replaced.

In normal condition, the bearing seat is divided into upper and lower sections, which are fastened together with bolts. To simulate SAGE, iron spacers with thicknesses of 0.1 mm, 0.2 mm, and 0.3 mm are inserted between the bearing seats at both ends. The distance of rotor elevation is the length of PMSG air-gap change, that is, the degree of SAGE faults.

In addition, under normal circumstances, the bearing inner ring has a uniform thickness and rotates with the rotor. To induce DAGE, 3D-printed inner rings with varying thicknesses are fabricated and substituted for the regular inner ring. This action causes the rotation center (O_1) of the PMSG rotor and its geometric center (O_2) to no longer align, thereby introducing a DAGE fault [27]. The degree of DAGE fault is contingent on the offset distance of the contour line in the 3D-printed inner ring, which is set at 0.1 mm, 0.2 mm, and 0.3 mm, respectively.

Ten operating conditions were carried out in the FEA and experiment, namely: Normal, SAGE0.1, SAGE0.2, SAGE0.3, DAGE0.1, DAGE0.2, DAGE0.3, SAGE0.1&DAGE0.1, SAGE0.1&DAGE0.2, SAGE0.2&DAGE0.2. The numbers following “SAGE” and “DAGE” indicate the magnitude of eccentricity in millimeters.

3.1.2. FEA and experimental results

Figs. 9–11 depict the FEA results, providing information on the spatial distribution, time-domain characteristics and frequency-domain characteristics of winding EF under various working conditions. Fig. 12 and Fig. 13 illustrate the time-domain and frequency-domain graphs of the vibration of the end winding in the experiment. However, it is noted

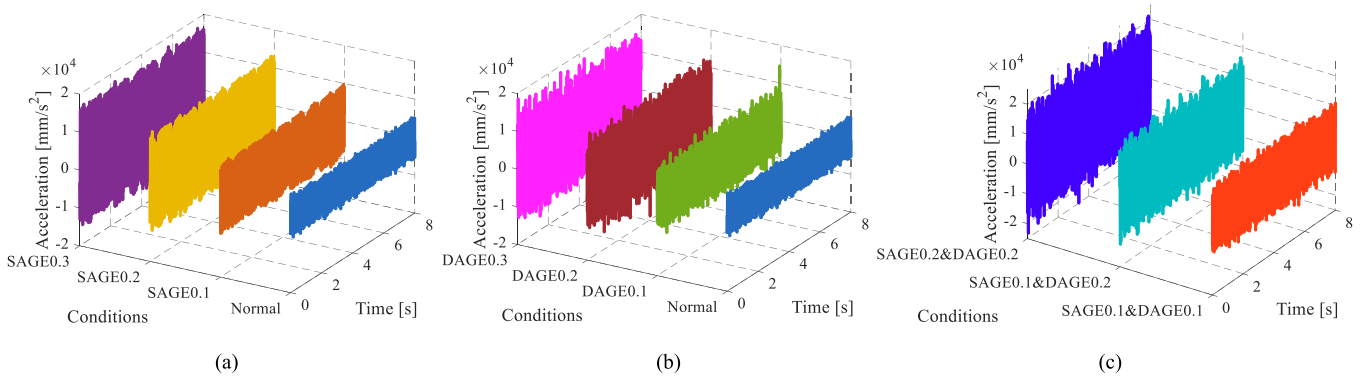

Fig. 13. Time domain of end winding vibration (a) Normal and SAGE, (b) Normal and DAGE, (c) HAGE.

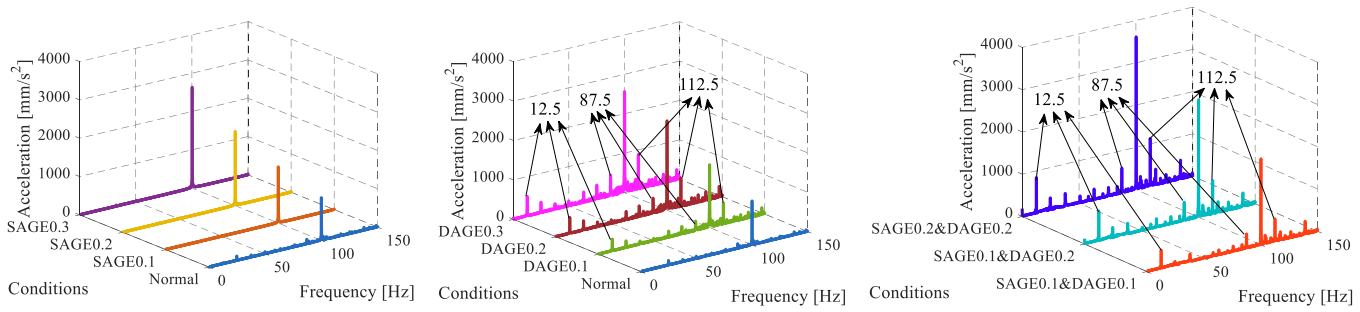

(a) (b) (c)

Fig. 14. Frequency domain of end winding vibration (a) Normal and SAGE, (b) Normal and DAGE, (c) HAGE.

Table 2
The amplitude of winding EF and end winding vibration frequency components under various working conditions.

Condition	Winding EF [mN]				End Winding Vibration [mm/s^2]				Trend
Frequency	12.5 Hz	87.5 Hz	100 Hz	112.5 Hz	12.5 Hz	87.5 Hz	100 Hz	112.5 Hz	
Normal	-		140.5	-	-		1110	-	increase
SAGE0.1			166.8				1461		
SAGE0.2			187.3				1932		
SAGE0.3			209.8				2631		
DAGE0.1	11.5	5.9	152.7	9.3	297	244	1586	532	increase
DAGE0.2	23.2	11.7	154.3	18.8	403	382	2258	724	
DAGE0.3	34.4	17.3	156.7	28.1	496	522	2558	880	
SAGE0.1&DAGE0.1	13.1	6.6	168.9	10.7	425	332	2028	526	increase
SAGE0.1&DAGE0.2	30.1	13.6	179.9	20.1	700	429	2772	784	
SAGE0.2&DAGE0.2	31.5	16.1	190.1	25.8	840	583	3608	1126	

that due to experimental limitations, the vibration distribution experiment for each winding was not conducted.

Fig. 9 presents the distribution of root-mean-square (RMS) values of the EF in the 48 stator end windings. The blue dotted lines on the graph represent the EF amplitude coordinates, and the unit is in millinewtons (mN). The numbers on the outermost ring correspond to the numbers of the windings (ranging from 1 to 48).

The information from Fig. 9(a) and (b) indicates that under normal condition, the EF in each end winding is approximately equal, forming a circular pattern. The occurrence of SAGE faults results in an uneven distribution of EF. Specifically, the EF amplitude decreases in areas where the air-gap increases, and it increases where the air-gap decreases, as shown in Fig. 9(a). Moreover, the magnitude of these changes becomes more pronounced as the SAGE degree deepens. After DAGE, the EF amplitude of each end winding uniformly increases, and this increase becomes more significant with a higher degree of DAGE, as depicted in Fig. 9(b). In Fig. 9(c), it is evident that HAGE is a combination of the effects of SAGE and DAGE, with each having a relatively independent influence on the EF amplitude. More specifically, when the SAGE degree remains unchanged, the EF amplitude increases uniformly with the deepening of DAGE. When the degree of DAGE is held constant, the EF distribution becomes more uneven as the SAGE degree deepens. These EF distribution results align with the theoretical derivations presented in Fig. 2.

The FEA results in Figs. 10–12 are based on the analysis of winding 1. Fig. 10 shows that both SAGE and DAGE increase the amplitude of end winding EF. In the normal state, the EF has a frequency component consisting of a DC component and 100 Hz (2 f). SAGE only affects the amplitude of each frequency component of EF without impacting the frequency components itself, as indicated in Fig. 11 (a). However, DAGE introduces new sideband frequency components of 12.5 Hz, 87.5 Hz and 112.5 Hz (f_r, 2 $f \pm f_r$) to EF, as shown in Fig. 11 (b). The frequency components of HAGE faults are consistent with those of DAGE faults, as seen in Fig. 11 (c). Additionally, the amplitude of EF frequency

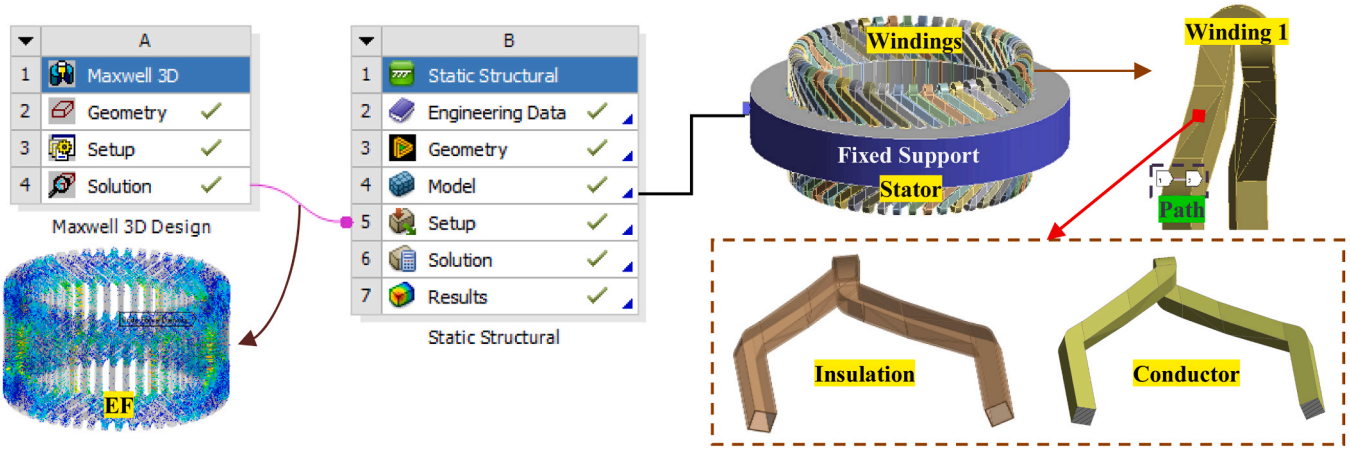

Fig. 15. Stress and strain calculation setup.

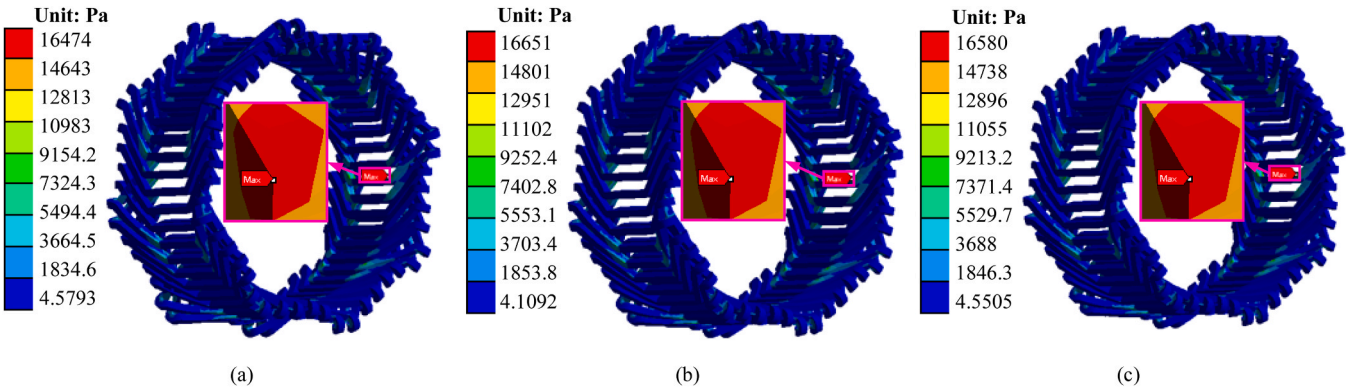

Fig. 16. Stress distribution of multiple windings (a) Normal, (b) SAGE0.1, (c) DAGE0.1.

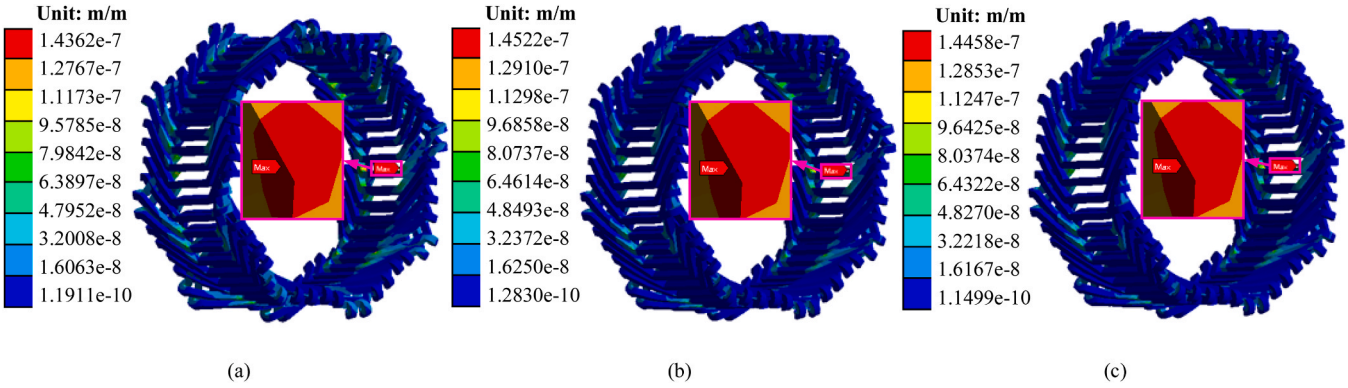

Fig. 17. Strain distribution of multiple windings (a) Normal, (b) SAGE0.1, (c) DAGE0.1.

Table 3
Maximum stress and strain of stator winding under each condition.

Conditions	Normal	SAGE0.1	SAGE0.2	SAGE0.3	DAGE0.1	DAGE0.2	DAGE0.3	S0.1D0.1	S0.1D0.2	S0.2D0.2
Stress [Pa]	16474	16651	16740	16835	16580	16669	16705	16682	16782	16910
Strain [10^{-7} m/m]	1.4362	1.4522	1.4602	1.4683	1.4458	1.4544	1.4582	1.4551	1.4641	1.4744
Trend	Low	→		High	Low	→	High	Low	→	High

components increases with the escalation of eccentric faults.

Fig. 12 compares the theory and FEA amplitude increments of EF at 12.5 Hz and 100 Hz. Particularly, in Fig. 12(a)-(c), the variation of the theoretical and FEA results under single SAGE, single DAGE and HAGE is based on the amplitude of the EF under SAGE0.3, DAGE0.3, and SAGE0.2&DAGE0.2. Additionally, the horizontal axis from 0 to 0.3 in Fig. 12(c) corresponds to Normal, SAGE0.1&DAGE0.1, SAGE0.1&DAGE0.2, and SAGE0.2&DAGE0.2 respectively. According to Fig. 12, the amplitude increments calculated by theoretical analysis and FEA in each working condition are consistent. In summary, the FEA results of EF in the time domain and frequency domain align with (6).

In a similar manner, the winding analyzed during the experiment is the section with the narrowest air-gap in the case of SAGE, which corresponds to winding 1 in the FEA model, and the results are shown in Fig. 13 and Fig. 14. In addition, the amplitudes of each frequency component from FEA and the experimental results were summarized, as shown in Table 2. The values of the left half represent the winding EF result from FEA, while the values of the right half are the end winding

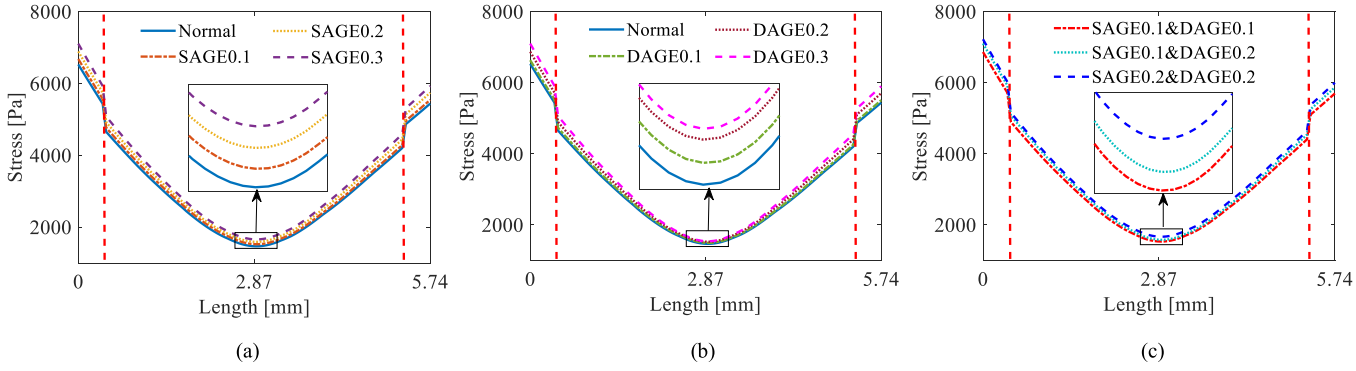

Fig. 18. Stress distribution along the path (a) Normal and SAGE, (b) Normal and DAGE, (c) HAGE.

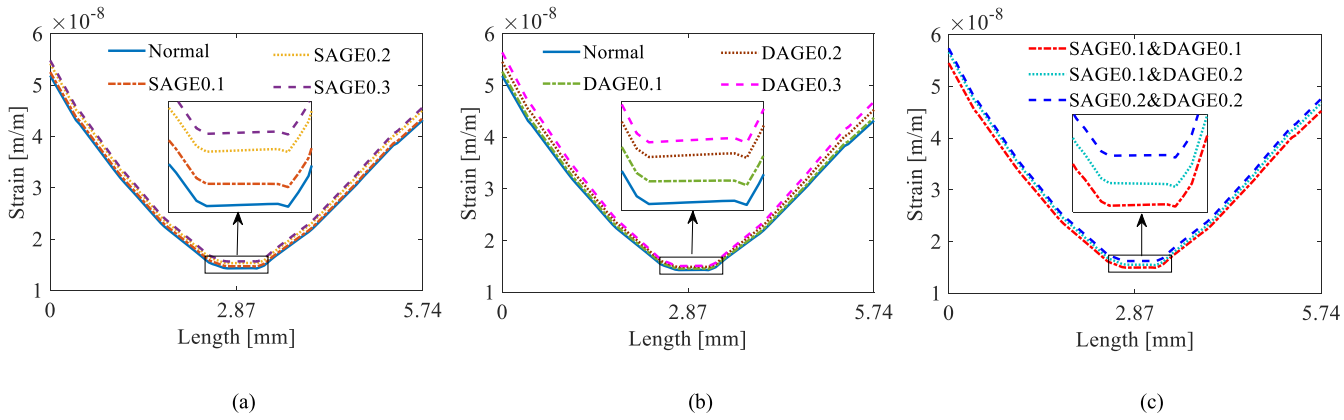

Fig. 19. Strain distribution along the path (a) Normal and SAGE, (b) Normal and DAGE, (c) HAGE.

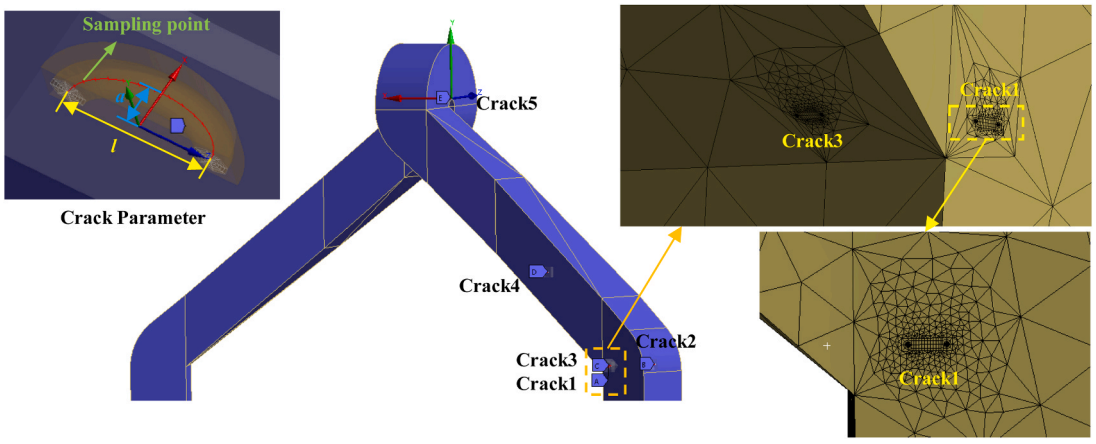

Fig. 20. Winding insulation crack setup.

vibration from the experiment.

According to Fig. 13, vibrations are present in the stator end winding under normal condition, and the occurrence of an eccentric fault increases the vibration amplitude. Specifically, the presence of SAGE fault increases the amplitude of the original frequency component (100 Hz), as shown in Fig. 14 (a). DAGE faults introduce new sideband frequency components to the end winding vibration, including 12.5 Hz, 87.5 Hz and 112.5 Hz (f_r and 2 $f\pm f_r$), as depicted in Fig. 14 (b). After HAGE, the end winding vibration frequency components align with those of DAGE, as illustrated in Fig. 14 (c). It is worth noting that the DC component of EF only causes the winding to deform without inducing vibration. Furthermore, the vibration of the end winding increases with the degree of eccentricity. The trend of amplitude variation for each frequency component under every experimental condition aligns with that observed in FEA, as illustrated in Table 2. In summary, the theoretical deductions, finite element analysis, and experimental outcomes are congruent.

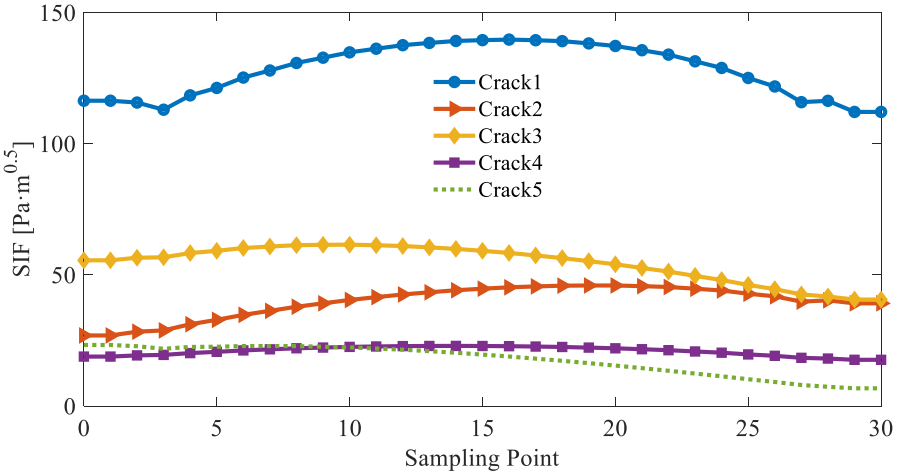

Fig. 21. Crack SIF at each position.

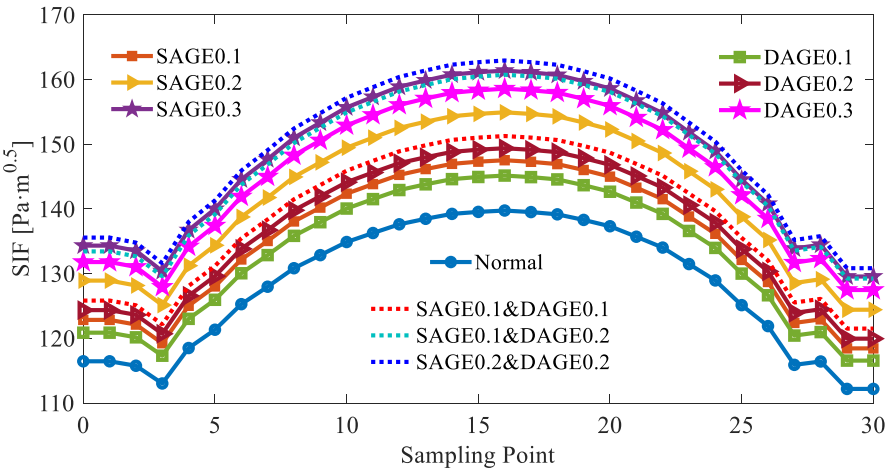

Fig. 22. Crack SIF under each condition.

3.2. Stress and strain verification of end windings

3.2.1. FEA setup

Fig. 15 illustrates the FEA setup for calculating the stress and strain distribution of the winding. The process involves importing the generator model and EF calculation results into the structural field in Ansys Workbench. To divide the winding into two parts, namely the insulation layer and copper rod, the imported geometric model should be modified within the structural part. This division results in the winding being divided into a thin shell and a solid core, each assigned different materials. The shell represents the insulating layer (made of mica), while the solid core beneath the shell signifies the copper rod (made of copper). The fixed part is the outer surface of the stator, and the winding is embedded in the slot of the stator. Additionally, a "Path" is set through the end winding to calculate the stress and strain along the path, as seen in Fig. 15. It's important to highlight that this "Path" is situated inside the winding rather than on its surface, traversing through both the insulation layer and the copper rod.

3.2.2. FEA results

Fig. 16 and Fig. 17 illustrate the stress and strain distribution in the winding subjected to EF. These figures reveal that the stress and strain distribution in single winding is similar across different working conditions. The maximum stress and strain are observed at the winding joint, aligning with the theoretical predictions. This occurs because the eccentric fault doesn't alter the distribution of EF within the winding, it merely affects the maximum/minimum values.

Table 3 provides information on the maximum stress and strain of the stator windings before and after eccentricity. It shows that the occurrence of eccentric faults leads to increased stress and strain in the windings, and these values increase with the severity of the fault. Notably, SAGE results in a more significant change in the maximum stress of the winding compared to the same degree of DAGE. This is due to the uneven distribution of EF under SAGE fault, resulting in larger stress and strain in a specific winding (winding 1). Under DAGE fault, EF is evenly distributed, and while the stress and strain of each winding increase compared to the normal condition, the maximum stress and strain amplitudes are lower than those of SAGE with the same degree of fault. It should be noted that the above "uneven" and "even" refer to the amplitude of the overall stress/strain of the different positions winding over a period of time, like the spatial distribution of the EF.

Fig. 18 and Fig. 19 depict the stress and strain distribution along the "Path", respectively. The thickness of the winding is 5.74 mm, with copper rods in the middle and insulation layer on both sides. The start point of "Path" is 0 mm on the horizontal coordinate shown in Figs. 18–19, and the end point is 5.74 mm.

In Fig. 18, it's worth noting that FEA exhibits a stress singularity issue, characterized by a sudden stress change at the junction of the insulation layer and the copper bar. This arises due to the difference in materials between the insulation layer of the winding and the copper rod. To provide more clarity, red dotted lines are used to distinguish the different materials in Fig. 18, with the insulation layer represented on both sides and the copper rod in the middle. Despite the appearance of the stress singularity problem, it's evident that the stress on the outer side (insulation layer) of the winding is the highest, while the stress on the inside is lower, as shown in Fig. 18. Regarding Fig. 19, FEA does not exhibit strain singularity. The distribution of strain amplitude along the "Path" mirrors that of stress, with smaller values in the middle and larger values on both sides. Furthermore, the local stress and strain within the winding increase with the deepening of the degree of eccentric fault, as demonstrated in Fig. 18 and Fig. 19. The results of stress and strain distribution are in agreement with the theoretical derivation.

3.3. Analysis of insulation failure with initial cracks

3.3.1. FEA setup

The semi-elliptical initial crack is set on the surface of the winding insulation layer, and then the load fracture behavior of the insulation with the initial crack is calculated, as shown in Fig. 20. The damage behavior of insulation in this study is characterized by SIF of cracks.

According to Fig. 20, the cracks were set at different parts of the end winding insulation layer, and the influence of different crack locations on the insulation fracture was calculated after the normal EF was introduced. The end winding is generally joint, involute part and nose end, as shown in Fig. 3(b). The three main parts all need to set cracks for comparison, and the joint should be paid more attention [17], so three cracks are set at the joint, located on different faces (the front of the joint is similar to the back, but the two sides are different). Hence there are 5 different crack locations, which are distributed in the front of the joint (Crack1), the side of the joint (Crack2 and Crack3), the middle of the involute (Crack4) and the nose (Crack5). In addition, in order to compare the SIF of cracks under different working conditions, EF under normal and different degrees of SAGE/DAGE/HAGE was introduced, and SIF of Crack1 was calculated.

In addition, the crack size also has an important effect on the insulation fracture behavior. As shown in Fig. 20, the crack size is mainly determined by two parameters: the crack depth (a) and the crack length (l). The SIF with different crack sizes is obtained by calculating Crack1 with different depths and lengths under normal condition. In order to compare SIF under different conditions, the horizontal coordinate is represented by sampling points uniformly (31 sampling points are taken for each crack).

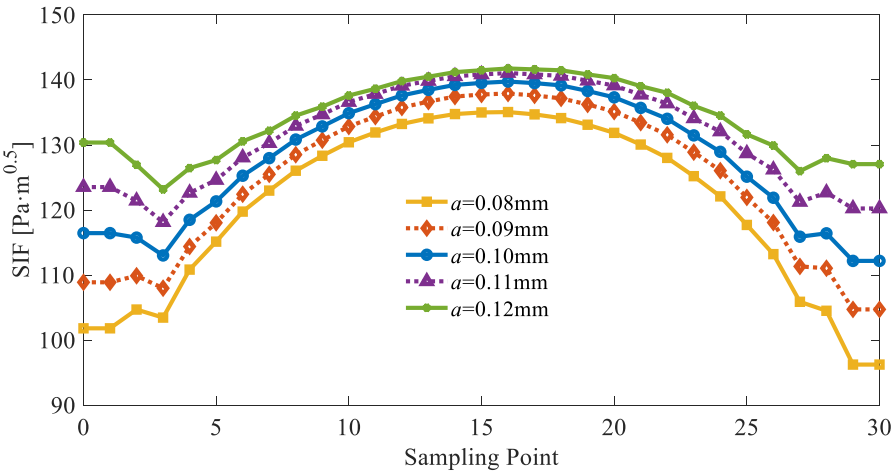

Fig. 23. Crack SIF under each depth.

3.3.2. FEA results

Fig. 21, Fig. 22, Fig. 23 and Fig. 24 display the calculated results pertaining to cracks at various positions, working conditions, depths and lengths.

As indicated by Fig. 21, when the crack is situated at the front of the joint (Crack1), the SIF is the highest, signifying the most significant damage to the insulation layer. Moreover, the SIF values of cracks located at the joint (Crack1, Crack2 and Crack3) are notably higher than those at other positions (Crack4 and Crack5), underscoring the joint as a critical area for the insulation layer that requires protective measures.

As illustrated in Fig. 22, it is evident that compared to normal condition, the SIF amplitude of Crack1 increases significantly under eccentric faults. The amplitude of SIF is greater with a more pronounced degree of eccentricity. Notably, when the degrees of SAGE and DAGE are the same, SAGE results in more substantial damage to winding 1.

Furthermore, Fig. 23 shows that, with a constant crack length (l_c=0.20 mm), SIF increases as the depth grows. Additionally, in Fig. 24, with a constant crack depth (a=0.10 mm), the SIF increases as the length of the crack extends. Therefore, enhancing both the depth and length of cracks will lead to an increase in SIF amplitudes.

4. Conclusion

This paper provides a comprehensive investigation into the mechanical properties and insulation damage of PMSG stator end windings, both before and after eccentricity. The findings of this study are as follows:

1) Under normal circumstances, EF of each winding is relatively consistent. However, SAGE faults lead to an uneven distribution of EF, while DAGE fault results in a uniform increase of EF in each winding. HAGE is the superposition of SAGE and HAGE. Furthermore, the vibration frequency components of PMSG stator end windings under normal and SAGE faults are 2 f, while the occurrence of DAGE and HAGE faults introduces new frequency components (f_r and 2 $f \pm f_r$). The amplitude of these frequency components increases with the severity of the fault.

2) Stress and strain are most pronounced at the winding joint. For a specific winding (the one with the smallest air-gap under SAGE fault), the stress and strain during SAGE are greater than those under the same level of DAGE. Additionally, the insulation layer, as the outermost component of the winding, experiences the most significant stress and strain within the same section.

3) The SIF amplitude of the crack at the winding joint, particularly the front part, is the most substantial and should be carefully monitored and protected. Moreover, the SIF amplitude of the crack increases with the fault severity, crack depth, and crack length.

This research offers valuable insights for PMSG state detection and fault diagnosis, and it serves as a reference for the analysis and optimization of the winding insulation layer.

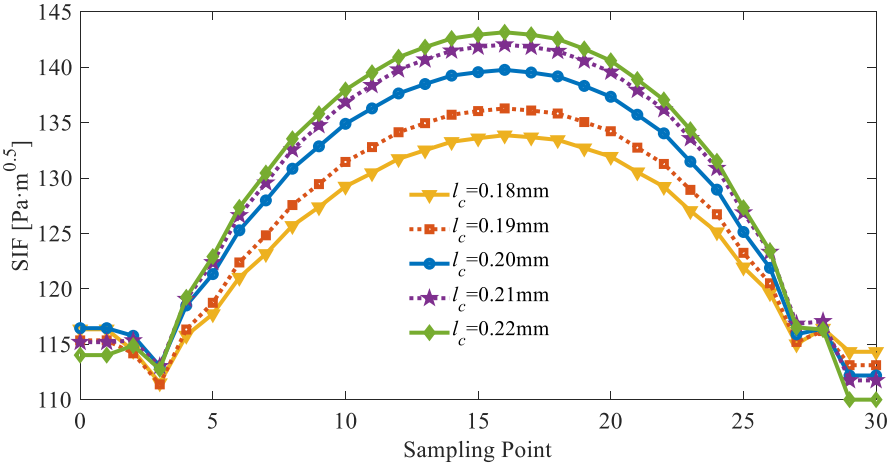

Fig. 24. Crack SIF under each length.

CRediT authorship contribution statement

De-Rui Dai: Writing – review & editing, Writing – original draft, Visualization, Validation, Supervision, Software, Methodology, Investigation, Formal analysis, Data curation. **David Gerada:** Software. **Zi-Xiang Fu:** Data curation. **Wen Zhang:** Writing – review & editing, Resources. **Ming-Xing Xu:** Writing – review & editing, Software, Resources. **Yu-Ling He:** Writing – review & editing, Resources, Project administration, Funding acquisition, Conceptualization.

Declaration of Competing Interest

No conflict of interest exits in the submission of this manuscript, and manuscript is approved by all authors for publication. We confirm that neither the manuscript nor any parts of its content are currently under consideration or published in another journal. All authors have approved the manuscript and agree with its submission to “Alexandria Engineering Journal”.

Acknowledgements

This work is supported by National Natural Science Foundation of China (52177042), the Chinese Fundamental Research Funds for the Central Universities (2023MS128), the Top Youth Talent Support Program of Hebei Province ([2018]-27), the High Level Talent Support Program of Hebei Province (B20231006), Post-Graduate’s Innovation Fund Project of Hebei Province (CXZZBS2023149) and Suzhou Social Developing Innovation Project of Science and Technology (SS202134).

References

[1] Sook Yee Yip, Hang Seng Che, Chee Pin Tan, Wen Tong Chong An, improved look-up table-based direct torque control for permanent magnet synchronous generator using Vienna rectifier, Int. J. Electr. Power Energy Syst. vol. 138 (2022) 107875.
[2] Ekamdeep Singh, Sajad Saraygord Afshari, Xihui Liang, Wind Turbine Optimal Preventive Maintenance Scheduling Using Fibonacci Search and Genetic Algorithm, J. Dyn., Monit. Diagn. vol. 2 (2023) 157–169.
[3] Amna Algolfat, Weizhuo Wang, Alhussein Albarbar, Damage identification of wind turbine blades - a brief review, J. Dyn., Monit. Diagn. vol. 2 (2023) 198–206.
[4] Ruibo Chen, Datong Qin, Changzhao Liu, Dynamic modelling and dynamic characteristics of wind turbine transmission gearbox-generator system electromechanical-rigid-flexible coupling, Alex. Eng. J. vol. 65 (2023) 307–325.
[5] Ester Sales-Setién, Ignacio Peñarrocha-Alós Robust, Robust estimation and diagnosis of wind turbine pitch misalignments at a wind farm level, Renew. Energy vol. 146 (2020) 1746–1765.
[6] Diako Azizi, Ahmad Gholami, Optimization of semiconductive coating and groundwall insulation layers in stator slot of HV generator, Int. J. Electr. Power Energy Syst. vol. 57 (2014) 384–391.
[7] B.K. Gupta, W.T. Fink, A proposed type test for interturn insulation in multi-turn coils. *Conference Record of the 1996*, IEEE Int. Symp. . Electr. Insul. (ISEI) vol. 1 (1996) 235–238.
[8] R. Lin, A.N. Laiho, A. Haavisto, A. Arkkio, End-winding vibrations caused by steady-state magnetic forces in an induction machine, IEEE Trans. Magn. vol. 46 (7) (2010) 2665–2674.
[9] J. Letal, B. Satmoko, N. Manik, G. Stone, Stator end-winding vibration in two-pole machines: avoiding generator failure, IEEE Ind. Appl. Mag. vol. 26 (6) (2020) 29–39.
[10] Bingjie Jing, Yanping Ling, Dongmei Wang, Erhang Zhu, Xiao Han, Analysis of transient electromagnetic force on end windings of 300 Mvar synchronous condenser during dynamic reactive power compensation process, Int. J. Electr. Power Energy Syst. vol. 155 (2024) 109538.
[11] Y. Zhao, B. Yan, C. Zeng, S. Huang, C. Chen, J. Deng, Optimal scheme for structural design of large turbogenerator stator end winding, IEEE Trans. Energy Convers. vol. 31 (4) (2016) 1423–1432.
[12] R. Albanese, F. Calvano, G. Dal Mut, et al., Coupled three dimensional numerical calculation of forces and stresses on the end windings of large turbo generators via integral formulation, IEEE Trans. Magn. vol. 48 (2) (2012) 875–878.
[13] J. Li, Y. Yang, W. Kong, Research on the stator end vibration characteristics of large generator sets, 2014 China Int. Conf. Electr. Distrib. (CICED) (2014) 461–464.
[14] P. Kung, L. Wang, M.I. Comanici, Stator end winding vibration and temperature rise monitoring, 2011 Electr. Insul. Conf. (EIC) (2011) 10–14.
[15] Ying Zhou, Qing-lei Zhang, Jian-guo Duan, Dynamical characteristics and influencing factors of stator end-windings of a turbine generator analyzed via heterogeneous element fusion modelling, Energy Rep. vol. 7 (2021) 658–672.
[16] Y. Fang, X. Bao, Q. lv, X. Cheng, Y. He, Analysis of electromagnetic force distribution on end winding of electrical submersible motor during starting transient operation, IEEE Trans. Magn. vol. 49 (2013) 5341–5345.
[17] Haijun Zhang, Mingjie Zhang, Xin Wang, Fracture failure analysis of insulation with initial crack defect for stator end-winding in induction motor by using magnetic-structural coupling model, Eng. Fail. Anal. vol. 149 (2023) 107239.
[18] M. Singh, A.G. Shaik, Incipient fault detection in stator windings of an induction motor using stockwell transform and SVM, IEEE Trans. Instrum. Meas. vol. 69 (12) (2020) 9496–9504.
[19] P. Zhang, D. Zheng, G. Lu, The effect and compensation of phase angle deviation along the winding for the online stator insulation condition monitoring, IEEE Trans. Ind. Electron. vol. 69 (8) (2022) 8440–8451.
[20] Bojan Jokanović, Milan Bebić, Nenad Kartalović, The influence of combined strain and constructive solutions for stator insulation of rotating electrical machines on duration of their reliable exploitation, Int. J. Electr. Power Energy Syst. vol. 110 (2019) 36–47.
[21] A. Siddique, G.S. Yadava, B. Singh, A review of stator fault monitoring techniques of induction motors (no), IEEE Trans. Energy Convers. vol. 20 (1) (2005) 106–114.
[22] X. Liu, J. Wang, R. Zhang, C. Xue, H. Chen, Y. Li, Electrical tree characteristics under AC and repetitive pulse voltages in wind turbine generator composite insulation, IEEE Trans. Dielectr. Electr. Insul. vol. 27 (3) (2020) 1007–1014.
[23] Prabhakar Neti, Pinjia Zhang, Xiaoguang Qi, et al., Online detection of endwinding contamination in industrial motors, 2011 Electr. Insul. Conf. (EIC) (2011) 265–270.
[24] K. Kimura, Y. Kaneda, The role of microscopic defects in multistress aging of micaceous insulation, IEEE Trans. Dielectr. Electr. Insul. vol. 2 (1995) 426–432.
[25] Xiaolin Chen, Yonghong Cheng, Bo Yue, et al., Study of epoxy/mica insulation deterioration in generator stator using ultra-wide band partial discharge testing technique, Polym. Test. vol. 25 (2006) 724–730.
[26] M. Aditya Gokhale, Subhakar, Singh Chetan, et al., Failure investigation of brazed copper winding bar strands of 250 MW stator, Eng. Fail. Anal. vol. 152 (2023) 107472.
[27] Yu-Ling He, De-Rui Dai, Ming-Xing Xu, et al., Experimental simulation and electromechanical characterization of dynamic air gap eccentricity faults in PMSG, IEEJ Trans. Electr. Electron. Eng. vol. 18 (2023) 1903–1913.
[28] Yu-Ling He, Yi-Fan Bai, Wen Zhang, et al., Impact of 3D air gap eccentricity on winding insulation temperature characteristic in PMSG, Alex. Eng. J. vol. 93 (2024) 220–235.
[29] Yu-Ling He, De-Rui Dai, Ming-Xing Xu, et al., Effect of static/dynamic air-gap eccentricity on stator and rotor vibration characteristics in doubly-fed induction generator, IET Electr. Power Appl. vol. 16 (2022) 1378–1394.
[30] Yao Da, Xiaodong Shi, Mahesh Krishnamurthy, A new approach to fault diagnostics for permanent magnet synchronous machines using electromagnetic signature analysis, IEEE Trans. Power Electron. vol. 28 (2013) 4104–4112.
[31] Yu-Ling He, Zhi-Jie Zhang, Wen-Qiang Tao, et al., A new external search coil based method to detect detailed static air-gap eccentricity position in nonsalient pole synchronous generators, IEEE Trans. Ind. Electron. vol. 68 (2021) 7535–7544.
[32] Harold Saavedra, Julio-C.ésar Urresty, Jordi-Roger Riba, Luís Romeral, Detection of interturn faults in PMSMs with different winding configurations, Energy Convers. Manag. vol. 79 (2014) 534–542.
[33] Viethung Nguyen, Danwei Wang, Jeevanand Seshadrinath, et al., A method for incipient interturn fault detection and severity estimation of induction motors under inherent asymmetry and voltage imbalance, IEEE Trans. Transp. Electrification vol. 3 (2017) 703–715.
[34] M. Pineda-Sanchez, M. Riera-Guasp, J. Perez-Cruz, et al., Transient motor current signature analysis via modulus of the continuous complex wavelet: a pattern approach, Energy Convers. Manag. vol. 73 (2013) 26–36.
[35] Bashir Mahdi Ebrahimi, Mohammad Etemadrezaei, Jawad Faiz, Dynamic eccentricity fault diagnosis in round rotor synchronous motors, Energy Convers. Manag. vol. 52 (2011) 2092–2097.
[36] E. Artigao, A. Honrubia-Escribano, E. Gómez-Lázaro, In-Service wind turbine DFIG diagnosis using current signature analysis, IEEE Trans. Ind. Electron. vol. 67 (2020) 2262–2271.
[37] Yu-Ling He, Yong Li, Wen Zhang, et al., Analysis of stator vibration characteristics in synchronous generators considering inclined static air gap eccentricity, IEEE Access vol. 11 (2023) 7794–7807.
[38] Wen Zhang, Yu-Ling He, Ming-Xing Xu, et al., A comprehensive study on stator vibrations in synchronous generators considering both single and combined SAGE cases, Int. J. Electr. Power Energy Syst. vol.143 (2022) 108490.
[39] Yu-Ling He, Yue-Xin Sun, Ming-Xing Xu, et al., Rotor UMP characteristics and vibration properties in synchronous generator due to 3D static air-gap eccentricity faults, IET Electr. Power Appl. vol. 14 (2020) 961–971.
[40] Ming-Xing Xu, Yu-Ling He, Wen Zhang, et al., Impact of radial air-gap eccentricity on stator end winding vibration characteristics in DFIG, Energies vol. 15 (2022) 6426.
[41] Alessandro Cimino, Frank Jenau, Andrey Mashkin, et al., Unidirectional accelerated lifetime investigations of mechanically dominated aged electrical insulation system used in generator winding bars, 2019 IEEE Electr. Insul. Conf. (EIC) (2019) 164–167.
[42] Alessandro Cimino, Frank Jenau, Christian Staubach, Causes of cyclic mechanical aging and its detection in stator winding insulation systems, IEEE Electr. Insul. Mag. vol. 35 (2019) 32–40.